ACS SENSORS

pubs.acs.org/acssensors

Article

Vitalizing Perovskite Oxide-Based Acetone Sensors with Metal–Organic Framework-Derived Heterogeneous Oxide Catalysts

Minhyun Kim,[§] Seyeon Park,[§] Jaewan Ahn, Jong Won Baek, Dong-Ha Kim, Hamin Shin, Jaehyun Ko, Lu Song, Chungseong Park, Euichul Shin, and Il-Doo Kim*

Cite This: *ACS Sens.* 2024, 9, 6492–6501

Read Online

ACCESS | Metrics & More | Article Recommendations | Supporting Information

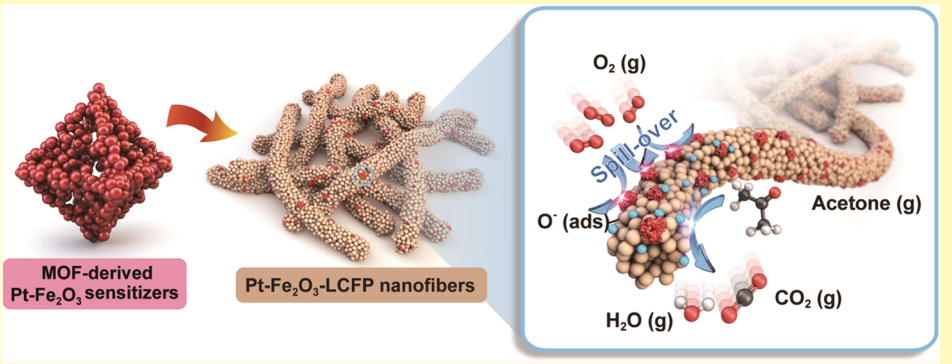

ABSTRACT: Perovskite oxides are promising candidates for chemiresistive-type gas sensors owing to their exceptional thermal and chemical stability during solid–gas reactions. However, perovskites suffer from critical issues such as low surface area and poor surface activity, which negatively influence the sensing characteristics. While metal nanoparticles can be incorporated in perovskites to improve their reactivity, the fundamental incompatibility between catalytic metals and perovskite oxides often leads to substantial structural degradation as well as phase instability. Herein, we overcome this challenge through the introduction of an intermediary phase that forms coherent interfaces with both the perovskite phase and catalyst metals. Specifically, we present the case study of p-type $La_{0.8}Ca_{0.2}Fe_{0.98}Pt_{0.02}O_3$ perovskite, whose hole accumulation layer was modulated by the incorporation of metal–organic framework (MOF)-derived n-type α-Fe_2O_3 nanoparticles decorated with highly dispersed Pt catalysts. The resulting composite exhibited significantly improved surface activity over the nonmodified $La_{0.8}Ca_{0.2}FeO_3$ perovskite, leading to exceptional chemiresistive sensing performance toward acetone gas (R_g/R_a = 39.8 toward 10 ppm of acetone at 250 °C) with high cross-sensitivity against interfering gases. Importantly, our findings reaffirm the critical influence of interfacial engineering in facilitating surface chemical reactions on perovskite oxides and, by doing so, effectively provide a general synthetic guideline to the design of perovskite-based chemiresistors.

KEYWORDS: *perovskite oxide, gas sensor, acetone sensor, semiconducting metal oxide, metal–organic framework*

Perovskite oxides have been considered a promising alternative to binary oxides owing to their high chemical stability for solid–gas reactions at high-temperature conditions and their excellent selectivity toward specific target analytes among interfering gases.[1−3] However, the clear advantages of perovskite oxides are overshadowed by their critically low sensitivity to chemical reactions, holding back their widespread adoption in chemiresistive gas sensing platforms. Specifically, the p-type nature of perovskites only provides limited variability in the carrier transport behavior from interaction with analyte gas molecules, even when doped with other elements, leading to low sensitivities and the inability to differentiate between different gas molecules.[4] The poor electronic properties also lead to an unclear understanding of the interfacial reactions between the gas molecules and the surface atoms of perovskite oxides, hampering the ability to fully exploit the material benefits in the design of high-performance gas sensors.

In this respect, the addition of sensitizing noble metal catalysts to perovskite oxides, which generate heterojunctions at the metal oxide interface for efficient charge transport, has been shown to improve the electronic properties of the perovskite.[5−10] While this strategy is promising for realizing perovskite-based high-performance gas sensors, incorporating

Received: July 23, 2024
Revised: October 16, 2024
Accepted: October 25, 2024
Published: November 1, 2024

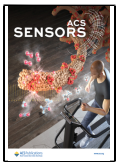

catalyst metals often destabilizes the perovskite lattice due to their low nonstoichiometric tolerance, significantly compromising their chemical activity.[11,12] Moreover, during repeated exposure to different target gases at elevated temperatures, the interplay of dopant atoms and noble metal nanoparticles also leads to undesired physical transformations that further mitigate the chemical activity.[10] To effectively circumvent these issues, we could conceive of introducing an intermediary layer that could coherently interface with both the perovskite lattice and the catalyst metal lattice to mitigate the phase instability. In this sense, heterojunctions formed between the perovskite and the intermediary, as well as the catalyst metal and the intermediary, must be able to facilitate efficient charge transfer.[13,14] Moreover, the total heterojunction area needs to be maximized for optimal sensitization, which can be achieved by designing the intermediary into nanocrystals that are uniformly distributed throughout the perovskite matrix, wherein the intermediary itself is homogeneously decorated with catalyst metal atoms.

Following these design principles, we report the preparation of $La_{0.8}Ca_{0.2}Fe_{0.98}Pt_{0.02}O_3$ (LCFP) perovskite oxide nanofibers decorated with Pt-dispersed α-Fe_2O_3 (Pt−Fe_2O_3) binary oxide nanoparticles as the intermediary layer supporting some amount of noble metal catalyst atoms. In this model system, the LCFP backbone was systematically investigated as $LaFeO_3$ derivatives exhibit high electrical conductivities and appropriate redox properties.[15−17] Moreover, Fe_2O_3 is known for its stable n-type semiconductor behavior, which, in combination with the chemical sensitization effect of Pt, significantly improves the electron transfer efficiency during the acetone sensing process with catalytic reliability. Herein, we first prepared the Pt−Fe_2O_3 nanograins by the pyrolysis of Pt-dispersed metal−organic framework (MOF) particles,[18] which were then incorporated in the LCFP matrix by an electrospinning-based oxide nanofiber synthesis protocol[19] for the production of Pt−Fe_2O_3-LCFP composite oxide nanofibers. Remarkably, our approach successfully preserved the structural and chemical properties of the host LCFP phase while significantly contributing to the interfacial effects between the guest Pt−Fe_2O_3 phase and the host LCFP phase. We demonstrated that the Pt−Fe_2O_3-LCFP exhibits an outstanding sensitivity toward acetone gas ($\Delta R/R_a$ = 39.8 toward 10 ppm of acetone at 250 °C), outperforming state-of-the-art perovskite-based acetone sensors due to the effective sensitization of the Pt−Fe_2O_3 catalyst. Importantly, Pt−Fe_2O_3 facilitated the adsorption of active oxygen species to provide sufficient reaction sites for the adsorption and desorption of acetone molecules. This meticulous report provides a refreshing perspective on the design of effective catalyst sensitizers on perovskite-based host materials for improving the sensing performance while maintaining their intrinsic durability.

EXPERIMENTAL SECTION

Materials. Poly(vinylpyrrolidone) (PVP, M_w = 1 300 000 g mol^{-1}), lanthanum(III) nitrate hexahydrate ($La(NO_3)_3·6H_2O$, 99.99%), calcium nitrate tetrahydrate ($Ca(NO_3)_2·4H_2O$, ACS reagent, 99%), iron(III) nitrate nonahydrate ($Fe(NO_3)_3·9H_2O$, ACS reagent, ≥98%), tetraammineplatinum(II) nitrate ($[Pt(NH_3)_4](NO_3)_2$, 99.995%, trace metals basis), and iron(III) chloride hexahydrate ($FeCl_3·6H_2O$) were purchased from Sigma-Aldrich (St. Louis). Terephthalic acid(C_6H_4-1,4-$(CO_2H)_2$, >99%) was purchased from Acros Organics. *N*,*N*-Dimethylformamide (DMF, 99.9%, SGR grade) was purchased from Daejung Chemicals & Metals. Ethyl alcohol (anhydrous, >99.9%) was supplied from Samchun Chemicals. All chemicals were used without further purification.

Metal−Organic Framework (MOF)-Mediated Synthesis of α-Fe_2O_3 and Pt-Dispersed α-Fe_2O_3 (Pt−Fe_2O_3) Nanoparticles. MIL-101(Fe) and Pt-dispersed MIL-101(Fe) were synthesized by modifying the previously reported protocol.[20] For the synthesis of MIL-101(Fe), 662 mg of $FeCl_3·6H_2O$ and 206 mg of terephthalic acid were dissolved in 15 mL of DMF. In the case of Pt-dispersed MIL-101(Fe), 9.48 mg of $[Pt(NH_3)_4](NO_3)_2$ was additionally dissolved in the same solution. This solution was stirred at 300 rpm and 3 h conditions. The mixed solution was transferred into a 30 mL Teflon-lined stainless-steel autoclave and kept at 120 °C for 12 h (ramping rate: 5 °C min^{-1}). After the autoclave was naturally cooled to room temperature, the product was washed and centrifuged once with DMF and three times with ethanol. The collected samples were dried at 60 °C. The dried powders were then subjected to calcination at 450 °C for 2 h (ramping rate: 5 °C min^{-1}) to obtain α-Fe_2O_3 and Pt−Fe_2O_3 nanoparticles. After the heat treatment, the samples were crushed with alumina balls for 3 min using vortex equipment for further usage.

Synthesis of $La_{0.8}Ca_{0.2}Fe_{0.98}Pt_{0.02}O_3$ (LCFP) and Pt−Fe_2O_3-Loaded $La_{0.8}Ca_{0.2}Fe_{0.98}Pt_{0.02}O_3$ (Pt−Fe_2O_3-LCFP) Nanofibers. To prepare LCFP and Pt−Fe_2O_3-LCFP electrospinning solution, 0.866 g of $La(NO_3)_3·6H_2O$, 0.118 g of $Ca(NO_3)_2·4H_2O$, 0.99 g of $Fe(NO_3)_3·9H_2O$, and 0.019 g $[Pt(NH_3)_4](NO_3)_2$ were dissolved in 10 mL of DMF. Then, the solution was vigorous stirring at a stirring speed of 300 rpm at room temperature for 1 h. 1.422 g of PVP was mixed with the solution and stirred under the same condition for at least 12 h. For preparing Pt−Fe_2O_3-LCFP electrospinning solution, 33, 50, and 100 mg of Pt−Fe_2O_3 powders were poured into the as-prepared solution above for 5.9, 8.9, and 17.7 wt % Pt−Fe_2O_3 compared to LCFP. Following vigorous stirring for at least 6 h, the color of the electrospinning solution turns from dark brown (the color of pristine LCFP electrospinning solution) to brick color, caused by the suspension of Pt−Fe_2O_3. The electrospinning solution was then transferred to a 24 mL syringe with a 23 G needle. The syringe was located at a distance of 15 cm from the collector, and the electrospinning was conducted at a direct current (DC) voltage of 15 kV and feeding rate of 20 μL min^{-1}. The as-spun nanofiber sheet was calcined at 450 °C for 2 h and 700 °C for 2 h (ramping rate: 5 °C min^{-1}) under static air. To control the mole ratios of Pt to Fe when preparing $La_{0.8}Ca_{0.2}Fe_{1-x}Pt_xO_3$, stoichiometric amounts of $Fe(NO_3)_3·9H_2O$ and $[Pt(NH_3)_4](NO_3)_2$ were dissolved. Specifically, we varied x from 0 to 0.03 and dissolved (1-x)·1.01 g of $Fe(NO_3)_3·9H_2O$ and x·0.968 g of $[Pt(NH_3)_4](NO_3)_2$ in the DMF-based electrospinning solution, following the same procedures for the electrospinning process and thermal treatment.

Material Characterization. X-ray diffraction (XRD) analysis (Rigaku SmartLab equipped with Cu Kα) was carried out at a scanning speed of 10° min^{-1} with a step size of 0.01° to study the crystal structures. The average crystallite sizes of (002), (123), and (202) reflections were calculated by the Scherrer equation as follows:

$$\tau = \frac{K\lambda}{\beta \cos\theta}$$

where τ is the mean size of crystalline domains, K is a dimensionless shape factor, λ is the wavelength of the incident beam, β is the line broadening factor at half of the maximum intensity (fwhm) in radian, and θ is the Bragg angle.

The surface morphology of the samples was analyzed by field-emission SEM (S4800, Hitachi). Atomic structural analysis, detailed surface morphology, and energy-dispersive spectrometry (EDS) mapping were carried out by Titan Double CS-corrected TEM (Titan cubed G2 60-300, FEI company). X-ray photoelectron spectroscopy analysis (Axis-Supra, Kratos, with Al Kα radiation) was conducted. The electronic band structures were confirmed by a UV−vis/NIR spectrophotometer (UV−vis, Lambda 1050, PerkinElmer) and a UV photoelectron spectrometer (UPS, K-Alpha+, Thermo). The absorbance of the material at 300−800 nm was provided through UV−vis spectroscopy, and the optical band gap was calculated using the obtained spectra. UPS analyzed the work function

https://doi.org/10.1021/acssensors.4c01852
ACS Sens. 2024, 9, 6492−6501

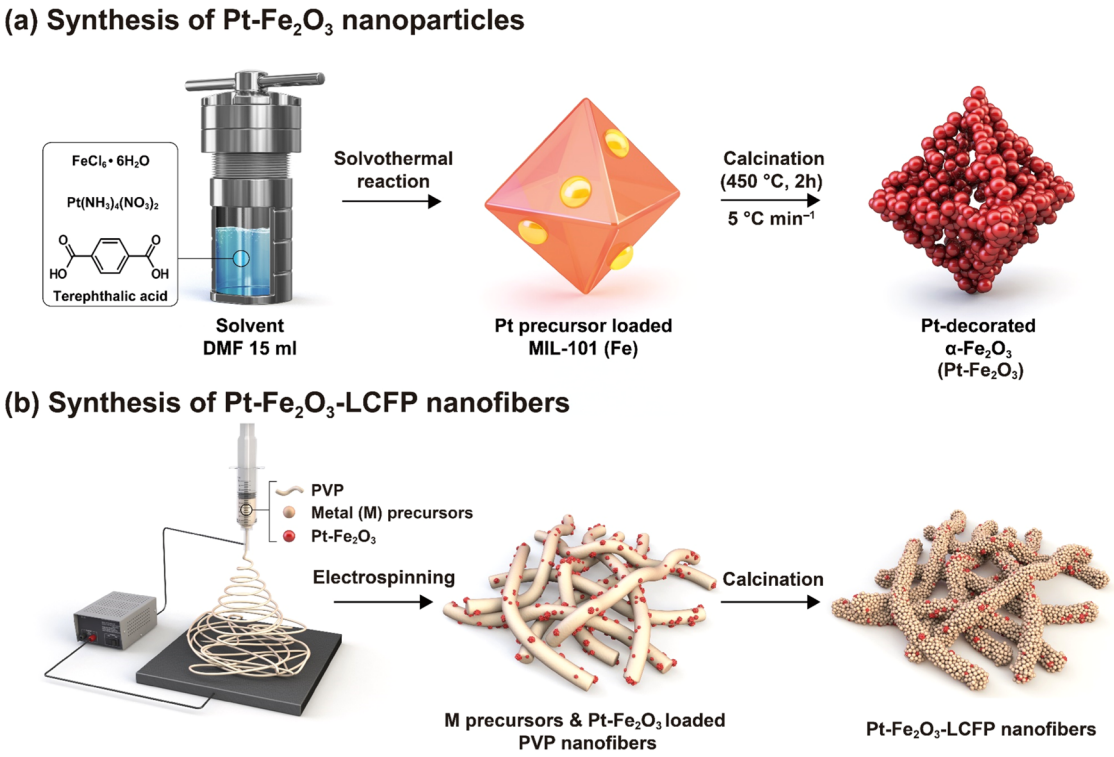

Figure 1. (a, b) Schematic illustration of the synthesis procedures to prepare Pt−Fe_2O_3 (a) and Pt−Fe_2O_3-LCFP (b).

and the valence band maximum (He I source with an energy of 21.2 eV, and in an energy step of 0.05 eV). Brunauer−Emmett−Teller (BET) surface area was measured with a Tristar II 3020 (Micromeritics). Inductively coupled plasma optical emission spectrometer (ICP-OES) analyses were conducted with a Thermo Scientific iCAP 6300 to quantify the molar ratios of Pt and Fe for a series of Pt−Fe_2O_3 samples.

Gas Sensing Tests. Dynamic resistance changes upon exposure to air and target analytes were measured to evaluate the sensing characteristics. To this end, the coating ink was prepared by dispersing 3 mg of the sample powder in 150 μL of ethanol, followed by ultrasonication for at least 3 min. Then, a 4 μL aliquot of the ink was drop-coated twice on the alumina substrate (2.5 × 2.5 mm^2) printed with two Au electrodes (width: 25 μm and electrode separation: 70 μm) on one side and Pt microheaters (heater resistance: 26.5 ± 0.5 Ω) on the backside. The temperature was controlled by a specific voltage applied to the microheater via a DC power supply (E3647A, Agilent). Before the target analytes were injected, the sensing materials were stabilized for 3 h in a dry air atmosphere. Then, a target analyte of a specific concentration was introduced into a sensor chamber at an interval of 10 min. The air was subsequently injected for recovery also at an interval of 10 min. The resistance was monitored with a data acquisition system (34972, Agilent) to measure changes for a 10 min response under a specific analyte and 10 min recovery under air.

RESULTS AND DISCUSSION

Figure 1 schematically illustrates the overall synthesis process to prepare $La_{0.8}Ca_{0.2}Fe_{0.98}Pt_{0.02}O_3$ (LCFP) nanofibers functionalized with Pt-dispersed α-Fe_2O_3 (Pt−Fe_2O_3). In a standard synthesis protocol, we first prepared Pt-dispersed MIL-101(Fe) by the solvothermal method, wherein the metal−organic framework (MOF) hosted the guest Pt precursor ions in its pores with a uniform distribution. Notably, MOFs serve as excellent precursors for creating metal−metal oxide composite catalysts, due to their highly porous structure, tunable compositions, and uniform metal distribution.[18,21] These characteristics allow for precise control over the size of metal nanoparticles during the pyrolysis process, resulting in enhanced catalytic activity and stability. Additionally, the porous structure of MOF-derived oxides improves effective gas diffusion and increases the availability of active sites, which is particularly advantageous for gas sensing reactions.[22] Upon calcination of the Pt-dispersed MIL-101(Fe), the Fe-based MOF structure was transformed into a porous Fe_2O_3 structure while the Pt species were formed into small clusters, resulting in the production of Pt−Fe_2O_3 (Figure 1a). In the next step, the as-obtained Pt−Fe_2O_3 were dispersed in a dimethylformamide-based poly(vinylpyrrolidone) (PVP) polymer solution containing the metal precursor ions (*i.e.*, La^{3+}, Ca^{2+}, Fe^{3+}, Pt^{2+}), which was electrospun into nanofibers. Calcination of these nanofibers occurred at temperatures high enough to fully remove the polymers, as determined by thermogravimetric analysis (TGA) and differential scanning calorimetry (DSC) data (Figure S1), yielded the LCFP perovskite nanofibers functionalized with Pt−Fe_2O_3 (Figure 1b).

We further established the synthesis mechanism of Pt−Fe_2O_3-LCFP nanofibers with the scanning electron microscopy (SEM) images of the samples corresponding to each synthesis step presented in Figure 2a−c that help to demonstrate the transformation of the materials. The as-prepared Pt-dispersed MIL-101(Fe) exhibited an octahedral polyhedral morphology with an average particle size of 780 nm (Figure S2). The subsequent calcination process decomposed the organic linkers and oxidized metal nodes to form a metal oxide phase, creating resultant metal oxide composite particles with sizes of 30−150 nm (Figure 2a). X-ray diffraction (XRD) showed the hematite phase over MOF-derived iron oxides after thermal annealing at 450 °C (Figure S3). The hematite phase was also validated for Pt−Fe_2O_3 calcined at 700 °C, where the LCFP perovskite oxide phase is generated, indicating high integrity at the elevated temperature without phase destruction. To demon-

https://doi.org/10.1021/acssensors.4c01852
ACS Sens. 2024, 9, 6492−6501

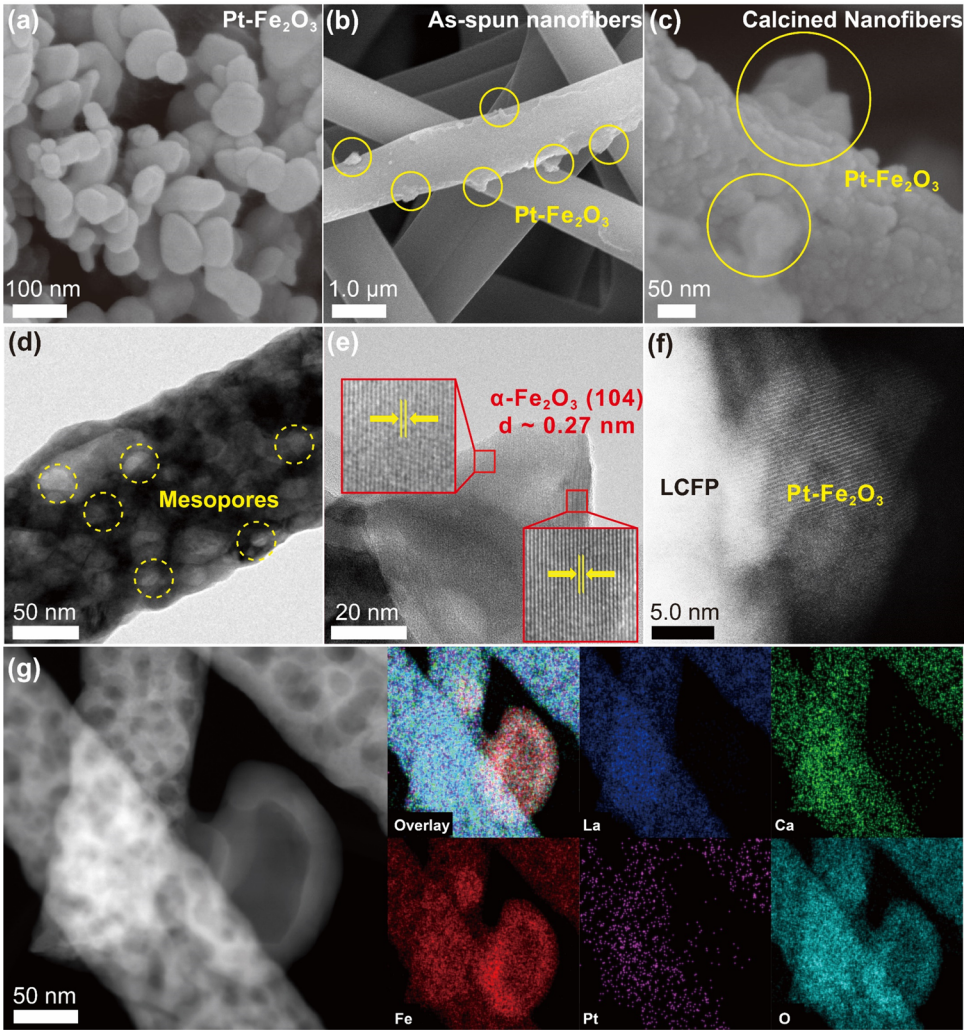

Figure 2. (a–c) SEM images of Pt–Fe_2O_3 (a), as-spun Pt–Fe_2O_3-LCFP nanofibers (b), and calcined Pt–Fe_2O_3-LCFP nanofibers (c). (d–f) HR-TEM images of Pt–Fe_2O_3-LCFP nanofiber (d) and Pt–Fe_2O_3 from Pt–Fe_2O_3-LCFP (e), and the high-magnitude STEM image of Pt–Fe_2O_3-LCFP nanofibers. (g) STEM image and EDS mapping results of Pt–Fe_2O_3-LCFP nanofibers.

strate the presence of Pt in the Pt–Fe_2O_3 composite, we quantitatively compared the molar ratio of Pt and Fe at each MOF-based synthesis step using inductively coupled plasma optical emission spectrometry (ICP-OES) analyses. As shown in Table S1, the molar ratios of Pt to Fe were maintained without significant differences across the synthesis steps. Next, the as-spun PVP-based composite nanofiber exhibited a uniform distribution of the nanometer-sized Pt–Fe_2O_3 throughout the nanofiber structure (Figure 2b). The fine distribution of Pt–Fe_2O_3 particles was preserved even on the LCFP nanofibers obtained after the polymer template was removed and the metal precursors were converted into the LCFP perovskite (Figure 2c). These composite nanofibers possessed mesopores (Figure 2d) due to the volume lost from the removal of the polymer. The lattice parameters of the LCFP nanofibers and anchored Pt–Fe_2O_3 were estimated to be 0.39 and 0.27 nm, respectively (Figures S4 and 2e). These values correspond to the interplanar distance of the (111) plane of LCFO nanofibers and the (104) plane of α-Fe_2O_3 crystallite.[23,24] At the same time, Pt–Fe_2O_3 showed a high dispersion of Pt species on the α-Fe_2O_3 lattice (Figure 2f) without significant aggregation of the noble metal as observed from a high-angle annular dark-field scanning transmission microscopy (HAADF-STEM) image. EDS mapping results further validated the high dispersion of Pt and Fe within Pt–Fe_2O_3 particles while also corroborating the uniform distribution of La, Ca, Fe, Pt, and O elements throughout the perovskite oxide nanofibers (Figure 2g). Altogether, our approach could successfully produce Pt–Fe_2O_3-LCFP composite nanofibers that could be used as a sensing layer.

Moreover, we studied the evolution of the interfaces between Pt–Fe_2O_3 and LCFP phases in the composite nanofibers by monitoring the changes in their structure as a function of loading of Pt–Fe_2O_3 particles. Specifically, we compared the detailed morphologies of the composite as the amount of Pt–Fe_2O_3 was controlled to be 5.9, 8.9, and 17.7 wt % relative to that of the LCFP perovskite oxide. XRD patterns in Figure 3a clearly show a linear increase in the intensity of characteristic peaks assigned to α-Fe_2O_3 as a function of the amount of Pt–Fe_2O_3, while the peaks corresponding to orthorhombic-structured $La_{0.8}Ca_{0.2}FeO_3$ perovskite phases showed little variation across all samples. The average crystallite sizes of the host oxide, calculated by the Scherrer equation, also remained stable in the range of 22–27 nm (Figure 3b). On these bases, we could conclude that Pt–Fe_2O_3 particles were successfully functionalized on LCFP nanofibers

https://doi.org/10.1021/acssensors.4c01852
ACS Sens. 2024, 9, 6492–6501

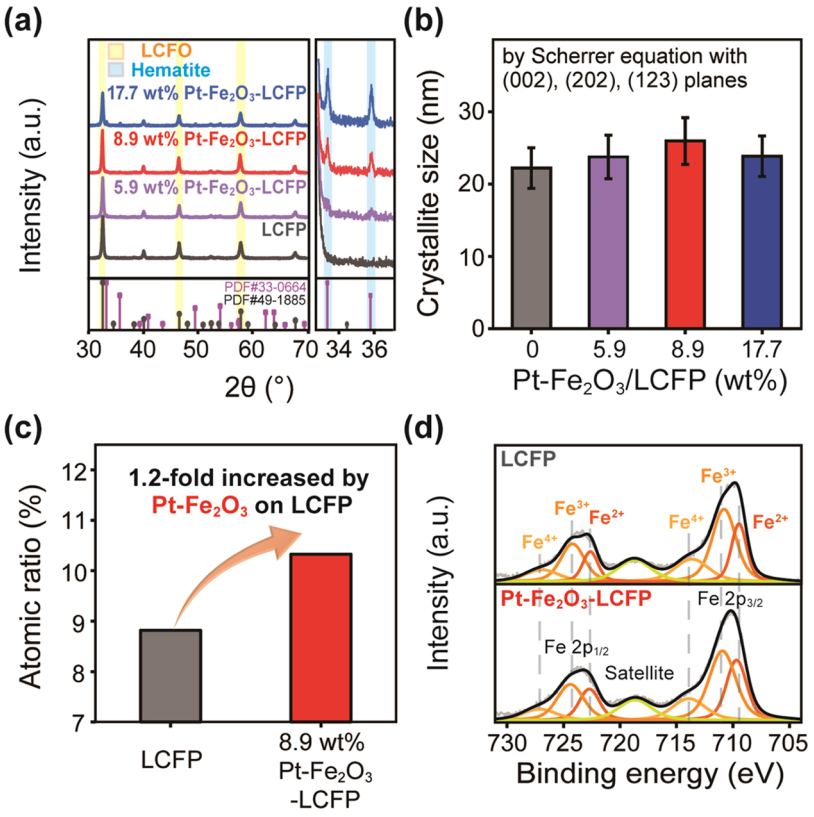

Figure 3. (a, b) X-ray diffraction (XRD) patterns (a) and the corresponding average crystallite sizes (b) of LCFP samples loaded with a controllable amount of Pt−Fe_2O_3. (c, d) High-resolution XPS analysis results for surface atomic ratio of Fe (c) and Fe 2p spectra (d) over LCFP and Pt−Fe_2O_3-LCFP samples.

without significantly disrupting the perovskite structure of the host LCFP. In addition, we found that the composite nanofibers possess larger surface areas (LCFP: 13 m^2 g^{-1}, and 8.9 wt % Pt−Fe_2O_3-LCFP: 10 m^2 g^{-1}) than the perovskite oxides prepared by conventional methods (0.25−2 m^2 g^{-1}).[25,26] This structural advantage of the oxide nanofibers leads to thicker hole accumulation layers at the nanometer-sized grains,[27] and helps target analytes readily diffuse onto large-surface-area sensing layers.[28−30]

We also utilized X-ray photoelectron spectroscopy (XPS) analyses to track the changes in the chemical state of Fe of the composite system (Figure 3c). To this end, for consistency, we discuss the atomic proportion of Fe within the whole structure (*i.e.*, comprising La, Ca, Fe, Pt, and O). Upon incorporating Pt−Fe_2O_3 particles into the LCFP, the surface Fe ratio increased from 8.8 to 10.3 atom %, which accounts for the additional Fe from the Pt−Fe_2O_3 particles. Notably, this also affected the Fe^{2+}/Fe^{3+} peak intensity ratio indicating the dissimilarity in the nature of Fe species in the Pt−Fe_2O_3 compared with those in the LCFP matrix. For reference, Fe^{2+}, Fe^{3+}, and Fe^{4+} were located at 709.6, 710.9, and 713.8 eV, respectively (Figure 3d). While the amount of Fe^{4+}/Fe^{3+} remained in a similar range (39% for Pt- Fe_2O_3-LCFP and 43% for LCFP), the Fe^{2+}/Fe^{3+} ratio significantly increased from 51 to 76% upon the addition of Pt−Fe_2O_3, indicating a steep increase in the Fe^{2+} species due to the presence of Pt−Fe_2O_3 (Table S2). The Fe species in Pt−Fe_2O_3 have lower Fe oxidation states than those in LCFP because the electron-rich Pt species (Figure S5) can donate electrons to α-Fe_2O_3, resulting in a significant deviation in the Fe oxidation states from the more stable Fe^{3+} state.[23,31]

Interestingly, Pt−Fe_2O_3 particles also affected the oxygen state of the composite surface. For this investigation, deconvolved XPS spectra for LCFP, 8.9 wt % Fe_2O_3-LCFP, and 8.9 wt % Pt−Fe_2O_3-LCFP samples were obtained and analyzed (Figure S6). Of the active oxygen species,[32−34] we specifically monitored the oxygen vacancy-related peak and the chemisorbed oxygen peak. We found that the relative abundance of the oxygen vacancy-related peak increased from 32.7% (LCFP) to 36.6% (Fe_2O_3-LCFP) and 39.0% (Pt−Fe_2O_3-LCFP), and that of the chemisorbed oxygen peak increased from 2.1% to 4.6 and 6.0%, respectively. Thus, the introduction of Fe_2O_3 particles increased the presence of reactive oxygen species, and the catalytic effect of Pt species further augmented the total amount of reactive oxygen species. All of these facts are indicative of the formation of n−p heterojunctions between dispersed Pt−Fe_2O_3 particles and the LCFP matrix. Ultimately, the density of active oxygen species at the heterojunctions makes the composite nanofibers more favorable for efficient gas sensing.[32]

We then comparatively evaluated the acetone detection performance of the Pt−Fe_2O_3-LCFP against pristine LCFP to investigate the effects of the engineered interfaces between the oxide sensitizer and the host perovskite oxide on sensing characteristics. Among various analytes, acetone is of particular interest as it is practically relevant for monitoring air quality and as a biomarker for exhaled breath diagnostics.[18,35] At an optimized measurement condition (Figure S7), we found that 8.9 wt % Pt−Fe_2O_3-LCFP exhibits a higher response at 250 °C ($\Delta R/R_a$ = 39.8 toward 10 ppm acetone) compared to the pristine LCFP nanofibers ($\Delta R/R_a$ = 3.5), and the composite sensing layer also showed a prominent selectivity toward

https://doi.org/10.1021/acssensors.4c01852
ACS Sens. 2024, 9, 6492−6501

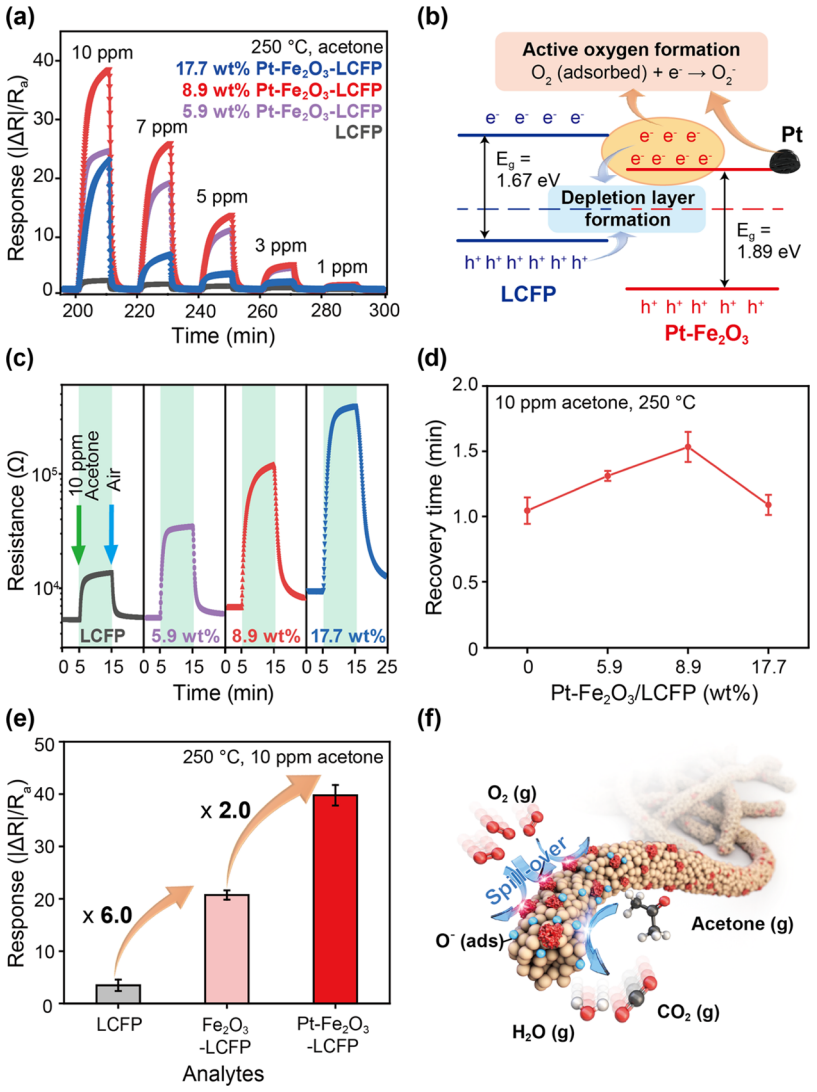

Figure 4. (a) Dynamic responses of LCFP loaded with a controllable amount of Pt−Fe_2O_3 particles toward 1−10 ppm acetone. (b) Band diagram of Pt−Fe_2O_3-LCFP and modeled carrier movement. (c, d) Comparison of baseline resistance (c) and recovery time (d) of Pt−Fe_2O_3-LCFP samples selectivity of 8.9 wt % Pt−Fe_2O_3-LCFP and LCFP to interfering gases (10 ppm) at 250 °C. (e) Comparison of acetone sensing characteristics of pristine LCFP, 8.9 wt % Fe_2O_3-LCFP, and 8.9 wt % Pt−Fe_2O_3-LCFP. (f) Schematic illustration of reaction mechanism between acetone gas and Pt−Fe_2O_3-LCFP.

acetone as shown in Figures 4a and S8. The enhanced sensing characteristics are explained by the accelerated oxygen spillover by the Fe_2O_3,[10,35] and with extra electrons provided by electron-rich Pt, the oxygen spillover phenomenon can be further facilitated to generate a greater number of adsorbed oxygen species. To quantify the adsorbed oxygen on sensing layers, we conducted temperature-programmed desorption of oxygen (O_2-TPD) experiments (Figure S9). The LCFP sensing layer functionalized with Fe_2O_3 exhibited stronger signals for both weakly adsorbed and strongly adsorbed oxygen species, compared to the pristine LCFP. The most prominent signals were observed in the Pt−Fe_2O_3-LCFP sample. This enhanced signal clearly demonstrates the increased oxygen adsorption capacity facilitated by the Pt−Fe_2O_3 sensitizer, significantly improving gas sensing reactions. Quantitative analyses revealed oxygen adsorption of 0.8, 1.1, and 1.4 $cm^3 g^{-1}$ for LCFP, Fe_2O_3-LCFP, and Pt−Fe_2O_3-LCFP, respectively. The adsorbed active oxygen species on oxide surfaces should react with acetone gas molecules following the equations below:[36]

$$O_2(g) + 2e^- \rightarrow 2O^-(ads) \quad (1)$$

$$CH_3COCH_3 + O^- \rightarrow CH_3COC^+H_2 + OH^- + e^- \quad (2a)$$

$$CH_3COCH_3 + 2O^- \rightarrow CH_3O^- + C^+H_3 + CO_2 + 2e^- \quad (2b)$$

$$e^- + h^+ \rightarrow (null) \quad (3)$$

The active oxygen species that reacted with acetone molecules at the n−p heterojunctions should decompose to carbon dioxide and water. However, if there is an excess of Pt−Fe_2O_3 particles to block the active interface area, the supply of reactive oxygen species becomes limited, resulting in weaker activities. Thus, a volcano-type relationship between the loading amount of Pt−Fe_2O_3 and acetone sensitivities was observed in Figure 4a. This phenomenon can be further elucidated through a band diagram of Pt−Fe_2O_3-LCFP (Figure 4b), constructed by estimating the band gap energies from Tauc plots and the work function as well as $E_F - E_{VBM}$ values

https://doi.org/10.1021/acssensors.4c01852
ACS Sens. 2024, 9, 6492−6501

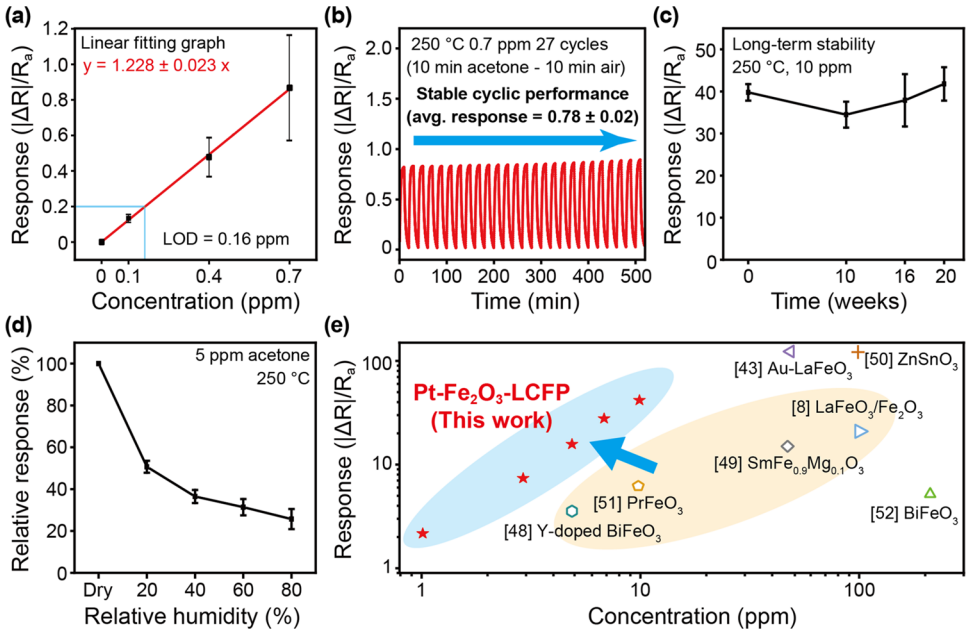

Figure 5. (a) Linear regression results of responses extracted from the response values toward sub-ppm-level (0.1, 0.4, and 0.7 ppm) acetone gases. (b) Dynamic responses upon cyclic exposure to 0.7 ppm acetone gas. (c, d) Long-term stability (c) and humidity test results (d) of Pt−Fe_2O_3-LCFP toward 5 ppm acetone gas. (e) Comparison of the response values to the state-of-the-art acetone sensors based on perovskite oxides.

from UV−vis/NIR spectrophotometry (UV−vis) and UV photoelectron spectrometry (UPS) analyses, respectively (Figure S10). In the equilibrium state, the band structure was representative of a typical type II heterojunction, wherein the electrons are preferentially transferred from LCFP to Pt−Fe_2O_3 and the holes from Pt−Fe_2O_3 to LCFP to achieve charge accumulation on each side. Charge carriers accumulated at the interface between Pt−Fe_2O_3 and LCFP promote active oxygen adsorption, which increases the frequency of reaction with acetone and ultimately improves acetone detection performance. Also, the electrons produced by these reactions between active oxygen species and acetone would recombine with electron holes on the primary sensing layer, LCFP. Therefore, the resistance would increase by a significant magnitude for each of the acetone molecules that interact with the active oxygen species on the surface of the composite sensing layer. However, as a side effect, the recombination at the heterojunction also creates carrier depletion layers. As depicted in Figure 4c, the carrier depletion layers were enlarged with an increasing amount of Pt−Fe_2O_3, which elevates the initial baseline resistance and, considering the p-type response of LCFP, compromises the sensitivity as a consequence. Empirically, we found that an 8.9 wt % loading of Pt−Fe_2O_3 could maximize the response of the LCFP ($\Delta R/R_a$ = 39.8), indicating that the aforementioned contrasting effects had been balanced. In this case, Pt−Fe_2O_3 could facilitate oxygen spillover at heterojunctions most effectively, surpassing the negative influence from charge carrier recombination. Indeed, when the loading was increased to 17.7 wt % Pt−Fe_2O_3, the excess electrons in the conduction band that did not participate in oxygen adsorption reactions had contributed more to decreasing the quantity of hole carriers while also expanding the carrier depletion layer, resulting in a decrease in the response ($\Delta R/R_a$ = 25.5). This relationship between the sensitivity and baseline resistance could also be supported by the trend in the recovery time of each sample (Figure 4d). The recovery time was gradually lengthened as the loading went up to 8.9 wt % Pt−Fe_2O_3 together with an improvement in the reactivity, since a larger amount of active oxygen species would require a greater number of surface sites to be recovered. In contrast, in the case of the 17.7 wt % Pt−Fe_2O_3-LCFP, the excessive electrons in the conduction band cut the recovery time shorter as these electrons restore the oxide surface more rapidly by facilitating reactions with oxygen.

In addition, the role of the Pt species in α-Fe_2O_3 as a catalytic sensitizer should also be rationalized. In the next set of experiments, therefore, for the same particle-basis loading of Pt−Fe_2O_3 at 8.9 wt %, we comparatively evaluated acetone sensing characteristics of the composite nanofibers with and without the presence of the Pt catalyst. Specifically, we prepared LCFP nanofibers, 8.9 wt % α-Fe_2O_3-decorated LCFP nanofibers (Fe_2O_3-LCFP), and 8.9 wt % Pt−Fe_2O_3-LCFP as shown in Figure 4e for this evaluation. The sensitivity of Fe_2O_3-LCFP to 10 ppm of acetone was increased by 6.0 times compared to that of pristine LCFP, representing the contribution from the heterojunctions. Interestingly, Pt−Fe_2O_3-LCFP exhibited a doubled sensitivity value compared to that of Fe_2O_3-LCFP, suggesting that Pt species specifically help create active-oxygen-rich interfaces that further react with acetone gas through a heterogeneous sensitization effect.[37] In fact, the deconvolved O 1s XPS spectra (Figure S5b,c) show that the cumulative area of active oxygen increased from 41.2% for pristine Fe_2O_3-LCFP to 45% for 8.9 wt % Pt−Fe_2O_3-LCFP. Therefore, Pt dispersed in the hematite catalyst enhanced its capacity for active oxygen formation, which is cited as a direct contributor to higher sensitivities.[36−39] Altogether, we visualize the overall reaction scheme in Figure 4f. Owing to this catalytic activity, the metal−metal oxide hybrid sensitizer was able to promote oxygen spillover while minimizing the blockage of the primary sensing layer and retaining its physical properties. Based on such a phenomenon, abundant reaction sites were available for reaction with acetone gases, leading to higher activity upon functionalization with Pt−Fe_2O_3.

https://doi.org/10.1021/acssensors.4c01852
ACS Sens. 2024, 9, 6492−6501

Having established that the composite perovskite sensing layer would exhibit high sensitivities to acetone based on these mechanisms, we further evaluated their viability as practical sensors based on a number of design criteria. The limit of detection (LOD) was estimated with a linear fitting of the response values toward several sub-ppm-level acetone gases, where we empirically set the reaction border as indistinguishable from the error when the resistance change does not exceed 20% of baseline resistance as frequently used in previous studies (Figure 5a).[40,41] The calculated LOD for Pt−Fe_2O_3-LCFP is 0.16 ppm, which is low enough to reliably distinguish a wide range of acetone concentrations under different health conditions. Specifically, acetone concentrations in healthy individuals range from 0.3 to 0.9 ppm, whereas it may increase to 1.8 ppm for diabetic patients.[42−44] This sensitivity enables the LCFP-based sensor to perform breath analysis with high efficiency, demonstrating its potential for practical use.

The stability of the Pt−Fe_2O_3-LCFP sample was validated by cyclic experiments and long-term stability tests. The sensing layer exhibited a stable performance ($|\Delta R|/R_a$ = 0.78) for 27 cycles of exposure to 0.7 ppm of acetone and recovery under air (Figure 5b). Also, we compared the sensing characteristics immediately after sensor fabrication and 10−20 weeks after the initial test, for which the response values for the aged sensor were maintained with a deviation of less than 15% from the initial response value, of which the average response value was 38.5 ± 3.1 toward 10 ppm of acetone (Figure 5c). The microstructure of the sample subjected to the long-term stability test was analyzed with SEM, TEM, and EDS mapping. As shown in Figure S11, the post-test sample exhibited no structural degradation or significant changes, maintaining nanofiber morphology similar to the as-prepared sample. Moreover, the EDS mapping results revealed that Pt−Fe_2O_3 was securely anchored on the LCFP scaffold. This high stability resulted from the structural advantage of the MOF-derived oxide catalyst that uniformly traps Pt atoms in pores, preventing their spontaneous sintering and deactivation.[18] The sensing performance was also tested under varied relative humidity (Figure 5d). Formation of surface hydroxyl groups on the oxide surface under highly humid environments typically degrades the sensitivity because more of the adsorbed oxygen species become unavailable for reaction. Nevertheless, the sensitivities can be improved by a humidity removal filter or catalytic overlayer that diminishes the interfering effects of water vapor.[44−47] Lastly, in similar operating conditions as other state-of-the-art perovskite-based acetone sensors, we confirmed that our composite sensor material showed significantly higher sensitivities (Figure 5e and Table S3).[8,43,48−52] Altogether, our design strategy provides a synthetic route to effectively address intrinsic issues of perovskite oxide-based sensors, improving their low sensitivities and also demonstrating the viability of the designed sensor material with high performance.

CONCLUSIONS

In this study, we demonstrated the interfacial engineering of perovskite oxide nanofibers by functionalizing metal/metal oxide composite sensitizers to form interphase heterojunctions that help modulate the surface chemistry of the sensing layer and enhance their sensitivities. Specifically, an abundance of n−p junctions was formed between the LCFP oxide nanofibers and the Pt−Fe_2O_3 nanoparticles that were coherently bound to the parent LCFP matrix with minimal surface blockage. The electrospinning process promoted the homogeneous distribution of the Pt−Fe_2O_3 nanoparticles over the LCFP nanofibers, successfully forming these active interfacial sites. Furthermore, the Pt species decorated on the n-type α-Fe_2O_3 served as chemical sensitizers to increase the electron density in the conduction band of the composite oxide, facilitating acetone sensing reactions. The resultant sensing performance of the heterogeneous oxide nanofiber showed significantly improved sensitivity toward acetone ($\Delta R/R_a$ = 39.8 ± 1.96 against 10 ppm of analyte) compared to the state-of-the-art acetone sensors based on perovskite oxides. The developed material also exhibited a lower detection limit (estimated 0.16 ppm) and stable sensing performance. Moreover, the composite showed exceptional stability owing to the structural benefits of the MOF-derived oxide catalyst that prevents sintering and deactivation. The central mechanism of the enhanced sensing performance can be ascribed to the accelerated oxygen spillover and vacancy formation induced by the Pt-decorated Fe_2O_3 sensitizers catalysts across the heterojunction, as well as the abundant presence of electrons participating in oxygen chemisorption. The increased number of active oxygen species provides sufficient reaction sites for acetone molecules, increasing the overall sensitivity. Altogether, our study established how the surface activity of perovskite oxide could be tuned by oxide sensitizers, facilitating favorable reactions for gas sensing, based on which we provide an effective fabrication method to generate heterojunction without degradation and increase catalytic activity for various chemical reactions.

ASSOCIATED CONTENT

Supporting Information

The Supporting Information is available free of charge at https://pubs.acs.org/doi/10.1021/acssensors.4c01852.

Additional characterization data for the as-spun nanofibers and calcined nanofibers (LCFP, Fe_2O_3-LCFP, Pt−Fe_2O_3-LCFP), including TGA-DSC, SEM, XRD, XPS, O_2-TPD, UPS, and ICP-OES analyses (PDF)

AUTHOR INFORMATION

Corresponding Author

Il-Doo Kim − *Department of Materials Science and Engineering, Korea Advanced Institute of Science and Technology (KAIST), Daejeon 34141, Republic of Korea;* orcid.org/0000-0002-9970-2218; Email: idkim@kaist.ac.kr

Authors

Minhyun Kim − *Department of Materials Science and Engineering, Korea Advanced Institute of Science and Technology (KAIST), Daejeon 34141, Republic of Korea*

Seyeon Park − *Department of Materials Science and Engineering, Korea Advanced Institute of Science and Technology (KAIST), Daejeon 34141, Republic of Korea;* orcid.org/0009-0009-2556-1449

Jaewan Ahn − *Department of Materials Science and Engineering, Korea Advanced Institute of Science and Technology (KAIST), Daejeon 34141, Republic of Korea;* orcid.org/0000-0002-0136-8427

Jong Won Baek − *Department of Materials Science and Engineering, Korea Advanced Institute of Science and Technology (KAIST), Daejeon 34141, Republic of Korea*

https://doi.org/10.1021/acssensors.4c01852
ACS Sens. 2024, 9, 6492−6501

Dong-Ha Kim − *Department of Materials Science and Engineering, Korea Advanced Institute of Science and Technology (KAIST), Daejeon 34141, Republic of Korea; Department of Materials Science and Chemical Engineering, Hanyang University, Ansan 15588, Republic of Korea*
Hamin Shin − *Department of Materials Science and Engineering, Korea Advanced Institute of Science and Technology (KAIST), Daejeon 34141, Republic of Korea*
Jaehyun Ko − *Department of Materials Science and Engineering, Korea Advanced Institute of Science and Technology (KAIST), Daejeon 34141, Republic of Korea*
Lu Song − *Department of Materials Science and Engineering, Korea Advanced Institute of Science and Technology (KAIST), Daejeon 34141, Republic of Korea*
Chungseong Park − *Department of Materials Science and Engineering, Korea Advanced Institute of Science and Technology (KAIST), Daejeon 34141, Republic of Korea*
Euichul Shin − *Department of Materials Science and Engineering, Korea Advanced Institute of Science and Technology (KAIST), Daejeon 34141, Republic of Korea*

Complete contact information is available at: https://pubs.acs.org/10.1021/acssensors.4c01852

Author Contributions

[§]M.K. and S.P. contributed equally to this work. M.K.: Materials synthesis and characterization, methodology, gas sensing test, data curation, validation, writing—original draft. S.P.: Project conceptualization, methodology, validation, formal analysis, writing—original draft. J.A.: Literature survey, validation, formal analysis, writing—reviewing and editing. J.W.B.: Material synthesis, validation, formal analysis. D.-H.K., H.S., J.K., L.S., C.P., E.S.: Validation, formal analysis. I.-D.K.: Funding acquisition, supervision, project conceptualization, data curation, validation, writing—reviewing and editing.

Notes

The authors declare no competing financial interest.

■ ACKNOWLEDGMENTS

This work was supported by the National Research Foundation of Korea (Grant No. RS-2024-00357296). This work was also supported by the Korea Technology and Information Promotion Agency for SMEs (Grant Nos. 00141845 and 00165289).

■ REFERENCES

(1) Bulemo, P. M.; Kim, I.-D. Recent advances in ABO_3 perovskites: Their gas-sensing performance as resistive-type gas sensors. *J. Korean Ceram. Soc.* **2020**, *57*, 24−39.
(2) Royer, S.; Duprez, D.; Can, F.; Courtois, X.; Batiot-Dupeyrat, C.; Laassiri, S.; Alamdari, H. Perovskites as substitutes of noble metals for heterogeneous catalysis: dream or reality. *Chem. Rev.* **2014**, *114* (20), 10292−10368.
(3) Kuhn, J. N.; Ozkan, U. S. Surface properties of Sr-and Co-doped $LaFeO_3$. *J. Catal.* **2008**, *253* (1), 200−211.
(4) Baek, J. W.; Kim, I.-D. Advances in Perovskite Oxides for Chemiresistive Sensors. *Acc. Mater. Res.* **2023**, *4* (12), 1108−1120.
(5) Sukee, A.; Alharbi, A.; Staerz, A.; Wisitsoraat, A.; Liewhiran, C.; Weimar, U.; Barsan, N. Effect of AgO loading on flame-made $LaFeO_3$ p-type semiconductor nanoparticles to acetylene sensing. *Sens. Actuators, B* **2020**, *312*, No. 127990.
(6) Zhang, H.; Qin, H.; Zhang, P.; Hu, J. High Sensing Properties of 3 wt% Pd-Doped $SmFe_{1-x}$ Mg_xO_3 Nanocrystalline Powders to Acetone Vapor with Ultralow Concentrations under Light Illumination. *ACS Appl. Mater. Interfaces* **2018**, *10* (18), 15558−15564.
(7) Zhou, T.; Zhang, T.; Zhang, R.; Lou, Z.; Deng, J.; Lu, G.; Wang, L. Constructing p−n heterostructures for efficient structure−driven ethanol sensing performance. *Sens. Actuators, B* **2018**, *255*, 745−753.
(8) Zhang, N.; Ruan, S.; Yin, Y.; Li, F.; Wen, S.; Chen, Y. Self-sacrificial template-driven $LaFeO_3/\alpha$-Fe_2O_3 porous nano-octahedrons for acetone sensing. *ACS Appl. Nano Mater.* **2018**, *1* (9), 4671−4681.
(9) Kang, J.-Y.; Jang, J.-S.; Koo, W.-T.; Seo, J.; Choi, Y.; Kim, M.-H.; Kim, D.-H.; Cho, H.-J.; Jung, W.; Kim, I.-D. Perovskite $La_{0.75}Sr_{0.25}Cr_{0.5}Mn_{0.5}O_{3-\delta}$ sensitized SnO_2 fiber-in-tube scaffold: highly selective and sensitive formaldehyde sensing. *J. Mater. Chem. A* **2018**, *6* (22), 10543−10551.
(10) Kim, Y.; Kim, H. S.; Kang, D.; Kim, M.; Lee, J. W. Enhanced redox performance of $LaFeO_3$ perovskite through in-situ exsolution of iridium nanoparticles for chemical looping steam methane reforming. *Chem. Eng. J.* **2023**, *468*, No. 143662.
(11) Malamis, S. A.; Harrington, R. J.; Katz, M. B.; Koerschner, D. S.; Zhang, S.; Cheng, Y.; Xu, L.; Jen, H.-W.; McCabe, R. W.; Graham, G. W. Comparison of precious metal doped and impregnated perovskite oxides for TWC application. *Catal. Today* **2015**, *258*, 535−542.
(12) Kothari, M.; Jeon, Y.; Miller, D. N.; Pascui, A. E.; Kilmartin, J.; Wails, D.; Ramos, S.; Chadwick, A.; Irvine, J. T. Platinum incorporation into titanate perovskites to deliver emergent active and stable platinum nanoparticles. *Nat. Chem.* **2021**, *13* (7), 677−682.
(13) Chu, J.; Han, K.; Yu, Q.; Wang, H.; Xi, K.; Lai, F.; Zhang, J.; Bao, Y. Schottky junction and multiheterostructure synergistically enhance rate performance and cycling stability. *Chem. Eng. J.* **2022**, *430*, No. 132994.
(14) Wang, C.; Zhang, X.; Yuan, B.; Wang, Y.; Sun, P.; Wang, D.; Wei, Y.; Liu, Y. Multi-heterojunction photocatalysts based on WO_3 nanorods: Structural design and optimization for enhanced photocatalytic activity under visible light. *Chem. Eng. J.* **2014**, *237*, 29−37.
(15) Cheng, G.; Tan, X.; Song, X.; Chen, X.; Dai, W.; Yuan, R.; Fu, X. Visible light assisted thermocatalytic reaction of CO + NO over $Pd/LaFeO_3$. *Appl. Catal., B* **2019**, *251* (15), 130−142.
(16) Thirumalairajan, S.; Girija, K.; Ganesh, I.; Mangalaraj, D.; Viswanathan, C.; Balamurugan, A.; Ponpandian, N. Controlled Synthesis of Perovskite $LaFeO_3$ Microsphere Composed of Nanoparticles via Self-Assembly Process and Their Associated Photocatalytic Activity. *Chem. Eng. J.* **2012**, *209*, 420−428.
(17) Patil, S. S.; Babar, B. M.; Nadargi, D. Y.; Shaikh, F. I.; Nadargi, J. D.; Sankapal, B. R.; Mulla, I. S.; Tamboli, M. S.; Troung, N. T. N.; Suryavanshi, S. S. La-Fe-O Perovskite Based Gas Sensors: Recent Advances and Future Challenges. *ACS Omega* **2024**, *9* (28), 29994−30014.
(18) Park, S.; Oh, D.; Ahn, J.; Kim, J. K.; Kim, D. H.; Kim, S.; Park, C.; Jung, W.; Kim, I. D. Promoting Ex-Solution from Metal−Organic-Framework-Mediated Oxide Scaffolds for Highly Active and Robust Catalysts. *Adv. Mater.* **2022**, *34* (27), No. 2201109.
(19) Baek, J. W.; Kim, Y. H.; Ahn, J.; Kim, D.-H.; Shin, H.; Ko, J.; Park, S.; Park, C.; Shin, E.; Jang, J.-S.; Kim, I. D. Galvanic replacement reaction in perovskite oxide for superior chemiresistors. *J. Mater. Chem. A* **2022**, *10* (43), 23282−23293.
(20) Yang, R. A.; Sarazen, M. L. Reaction pathways and deactivation mechanisms of isostructural Cr and Fe MIL-101 during liquid-phase styrene oxidation by hydrogen peroxide. *Catal. Sci. Technol.* **2021**, *11* (15), 5282−5296.
(21) Casells-Gil, J.; Ould-Chikh, S.; Ramírez, A.; Ahmad, R.; Prieto, G.; Gómez, A. R.; Garzón-Tovar, L.; Telalovic, S.; Liu, L.; Genovese, A.; Padial, N. M.; Aguilar-Tapia, A.; Bordet, P.; Cavallo, L.; Martí-Gastaldo, C.; Gascon, J. Unlocking mixed oxides with unprecedented stoichiometries from heterometallic metal-organic frameworks for the catalytic hydrogenation of CO_2. *Chem. Catal.* **2021**, *1* (2), 364−382.
(22) Jang, J.-S.; Koo, W.-T.; Choi, S.-J.; Kim, I.-D. Metal Organic Framework-Templated Chemiresistor: Sensing Type Transition from P-to-N Using Hollow Metal Oxide Polyhedron via Galvanic Replacement. *J. Am. Chem. Soc.* **2017**, *139* (34), 11868−11876.

(23) Almeida, T. P.; Fay, M.; Zhu, Y.; Brown, P. D. Process map for the hydrothermal synthesis of α-Fe_2O_3 nanorods. *J. Phys. Chem. C* **2009**, *113* (43), 18689−18698.
(24) Price, P. M.; Rabenberg, E.; Thomsen, D.; Misture, S. T.; Butt, D. P. Phase Transformations in Calcium-Substituted Lanthanum Ferrite. *J. Am. Ceram. Soc.* **2014**, *97* (7), 2241−2248.
(25) Si, C.; Zhang, C.; Sunarso, J.; Zhang, Z. Transforming bulk alloys into nanoporous lanthanum-based perovskite oxides with high specific surface areas and enhanced electrocatalytic activities. *J. Mater. Chem. A* **2018**, *6* (41), 19979−19988.
(26) Wang, Y.; Chi, Z.; Chen, C.; Su, C.; Liu, D.; Liu, Y.; Duan, X.; Wang, S. Facet-and defect-dependent activity of perovskites in catalytic evolution of sulfate radicals. *Appl. Catal., B* **2020**, *272*, No. 118972.
(27) Kim, H.-J.; Lee, J.-H. Highly sensitive and selective gas sensors using p-type oxide semiconductors: Overview. *Sens. Actuators, B* **2014**, *192*, 607−627.
(28) Li, B.-Q.; Xia, Z.-J.; Zhang, B.; Tang, C.; Wang, H.-F.; Zhang, Q. Regulating p-block metals in perovskite nanodots for efficient electrocatalytic water oxidation. *Nat. Commun.* **2017**, *8* (1), 934.
(29) Lai, X.; Shen, G.; Xue, P.; Yan, B.; Wang, H.; Li, P.; Xia, W.; Fang, J. Ordered mesoporous NiO with thin pore walls and its enhanced sensing performance for formaldehyde. *Nanoscale* **2015**, *7* (9), 4005−4012.
(30) Rothschild, A.; Komem, Y. The effect of grain size on the sensitivity of nanocrystalline metal-oxide gas sensors. *J. Appl. Phys.* **2004**, *95* (11), 6374−6380.
(31) Shi, C.; Qin, H.; Zhao, M.; Wang, X.; Li, L.; Hu, J. Investigation on electrical transport, CO sensing characteristics and mechanism for nanocrystalline $La_{1-x}Ca_xFeO_3$ sensors. *Sens. Actuators, B* **2014**, *190*, 25−31.
(32) Park, S.; Jeon, S.; Kim, H.; Philips, J.; Oh, D.; Ahn, J.; Kim, M.; Park, C.; Hong, S.; Kim, J. Imparting metal oxides with high sensitivity toward light-activated NO_2 detection via tailored interfacial chemistry. *Adv. Funct. Mater.* **2023**, *33* (17), No. 2214008.
(33) Khan, F. U.; Mehmood, S.; Liu, S.; Xu, W.; Shah, M. N.; Zhao, X.; Ma, J.; Yang, Y.; Pan, X. A pn Heterojunction based Pd/PdO@ZnO organic frameworks for high-sensitivity room-temperature formaldehyde gas sensor. *Front. Chem.* **2021**, *9*, No. 742488.
(34) Gandla, S.; Gollu, S. R.; Sharma, R.; Sarangi, V.; Gupta, D. Dual role of boron in improving electrical performance and device stability of low temperature solution processed ZnO thin film transistors. *Appl. Phys. Lett.* **2015**, *107* (15), No. 152102, DOI: 10.1063/1.4933304.
(35) Park, S.; Lim, Y.; Oh, D.; Ahn, J.; Park, C.; Kim, M.; Jung, W.; Kim, J.; Kim, I.-D. Steering selectivity in the detection of exhaled biomarkers over oxide nanofibers dispersed with noble metals. *J. Mater. Chem. A* **2023**, *11* (7), 3535−3545.
(36) Koo, W.-T.; Yu, S.; Choi, S.-J.; Jang, J.-S.; Cheong, J. Y.; Kim, I.-D. Nanoscale PdO catalyst functionalized Co_3O_4 hollow nanocages using MOF templates for selective detection of acetone molecules in exhaled breath. *ACS Appl. Mater. Interfaces* **2017**, *9* (9), 8201−8210.
(37) Koo, W.-T.; Choi, S.-J.; Kim, S.-J.; Jang, J.-S.; Tuller, H. L.; Kim, I.-D. Heterogeneous Sensitization of Metal−Organic Framework Driven Metal@Metal Oxide Complex Catalysts on an Oxide Nanofiber Scaffold Toward Superior Gas Sensors. *J. Am. Chem. Soc.* **2016**, *138* (40), 13431−13437.
(38) Park, S.; Bulemo, P. M.; Koo, W.-T.; Ko, J.; Kim, I.-D. Chemiresistive acetylene sensor fabricated from Ga-doped ZnO nanofibers functionalized with Pt catalysts. *Sens. Actuators, B* **2021**, *343*, No. 130137.
(39) Staerz, A.; Weimar, U.; Barsan, N. Current state of knowledge on the metal oxide based gas sensing mechanism. *Sens. Actuators, B* **2022**, *358*, No. 131531.
(40) Lee, C.-S.; Dai, Z.; Li, H.-Y.; Jo, Y.-M.; Kim, B.-Y.; Byun, H.-G.; Hwang, I.; Lee, J.-H. Highly discriminative and sensitive detection of volatile organic compounds for monitoring indoor air quality using pure and Au-loaded 2D In_2O_3 inverse opal thin films. *Sens. Actuators, B* **2018**, *273*, 1−8.
(41) Choi, H. J.; Chung, J.-H.; Yoon, J.-W.; Lee, J.-H. Highly selective, sensitive, and rapidly responding acetone sensor using ferroelectric ε-WO_3 spheres doped with Nb for monitoring ketogenic diet efficiency. *Sens. Actuators, B* **2021**, *338*, No. 129823.
(42) Lee, J. E.; Lim, C. K.; Park, H. J.; Song, H.; Choi, S.-Y.; Lee, D.-S. ZnO−CuO core-hollow cube nanostructures for highly sensitive acetone gas sensors at the ppb level. *ACS Appl. Mater. Interfaces* **2020**, *12* (31), 35688−35697.
(43) Shingange, K.; Swart, H.; Mhlongo, G. H. Ultrafast detection of low acetone concentration displayed by Au-loaded $LaFeO_3$ nanobelts owing to synergetic effects of porous 1D morphology and catalytic activity of Au nanoparticles. *ACS Omega* **2019**, *4* (21), 19018−19029.
(44) Kwak, C.-H.; Kim, T.-H.; Jeong, S.-Y.; Yoon, J.-W.; Kim, J.-S.; Lee, J.-H. Humidity-independent oxide semiconductor chemiresistors using terbium-doped SnO_2 yolk−shell spheres for real-time breath analysis. *ACS Appl. Mater. Interfaces* **2018**, *10* (22), 18886−18894.
(45) Liu, W.; Xu, L.; Sheng, K.; Zhou, X.; Dong, B.; Lu, G.; Song, H. A highly sensitive and moisture-resistant gas sensor for diabetes diagnosis with Pt@In_2O_3 nanowires and a molecular sieve for protection. *NPG Asia Mater.* **2018**, *10* (4), 293−308.
(46) Jeong, S. Y.; Moon, Y. K.; Kim, J. K.; Park, S. W.; Jo, Y. K.; Kang, Y. C.; Lee, J. H. A general solution to mitigate water poisoning of oxide chemiresistors: bilayer sensors with Tb_4O_7 overlayer. *Adv. Funct. Mater.* **2021**, *31* (6), No. 2007895.
(47) Zhu, X. J.; Chang, X. T.; Tang, S. K.; Chen, X. Q.; Gao, W. X.; Niu, S. C.; Li, J. F.; Jiang, Y. C.; Sun, S. B. Humidity-Tolerant Chemiresistive Gas Sensors Based on Hydrophobic CeO_2/SnO_2 Heterostructure Films. *ACS Appl. Mater. Interfaces* **2022**, *14* (22), 25680−25692.
(48) Neogi, S.; Ghosh, R. Origin of irreversible to reversible transition in acetone detection for Y-doped $BiFeO_3$ perovskite. *J. Appl. Phys.* **2020**, *128* (14), No. 144501, DOI: 10.1063/5.0023131.
(49) Liu, X.; Hu, J. F.; Cheng, B.; Qin, H. W.; Jiang, M. H. Acetone gas sensing properties of $SmFe_{1-x}Mg_xO_3$ perovskite oxides. *Sens. Actuators, B* **2008**, *134* (2), 483−487.
(50) Jiang, L. L.; Chen, Z. Y.; Cui, Q.; Xu, S.; Tang, F. L. Experimental and DFT-D3 study of sensitivity and sensing mechanism of $ZnSnO_3$ nanosheets to C_3H_6O gas. *J. Mater. Sci.* **2022**, *57* (5), 3231−3251.
(51) Ma, L.; Ma, S. Y.; Shen, X. F.; Wang, T. T.; Jiang, X. H.; Chen, Q.; Qiang, Z.; Yang, H. M.; Chen, H. $PrFeO_3$ hollow nanofibers as a highly efficient gas sensor for acetone detection. *Sens. Actuators, B* **2018**, *255*, 2546−2554.
(52) Yu, Q. C.; Zhang, Y. C.; Xu, Y. Hierarchical hollow $BiFeO_3$ microcubes with enhanced acetone gas sensing performance. *Dalton Trans.* **2021**, *50* (19), 6702−6709.

https://doi.org/10.1021/acssensors.4c01852
ACS Sens. 2024, 9, 6492−6501